LETTERS
PUBLISHED ONLINE: 21 NOVEMBER 2016 | DOI: 10.1038/NNANO.2016.248
nature nanotechnology

# Single-nanotube tracking reveals the nanoscale organization of the extracellular space in the live brain

Antoine G. Godin[1,2†], Juan A. Varela[3,4†], Zhenghong Gao[1,2†], Noémie Danné[1,2], Julien P. Dupuis[3,4], Brahim Lounis[1,2], Laurent Groc[3,4*] and Laurent Cognet[1,2*]

**The brain is a dynamic structure with the extracellular space (ECS) taking up almost a quarter of its volume[1,2]. Signalling molecules, neurotransmitters and nutrients transit via the ECS, which constitutes a key microenvironment for cellular communication[3] and the clearance of toxic metabolites. The spatial organization of the ECS varies during sleep[4], development[5] and aging[6] and is probably altered in neuropsychiatric and degenerative diseases[7], as inferred from electron microscopy[8,9] and macroscopic biophysical investigations[2,10]. Here we show an approach to directly observe the local ECS structures and rheology in brain tissue using super-resolution imaging. We inject single-walled carbon nanotubes into rat cerebroventricles and follow the near-infrared emission of individual nanotubes as they diffuse inside the ECS for tens of minutes in acute slices. Because of the interplay between the nanotube geometry and the ECS local environment, we can extract information about the dimensions and local viscosity of the ECS. We find a striking diversity of ECS dimensions down to 40 nm, and as well as of local viscosity values. Moreover, by chemically altering the extracellular matrix of the brains of live animals before nanotube injection, we reveal that the rheological properties of the ECS are affected, but these alterations are local and inhomogeneous at the nanoscale.**

Investigations of the fine structure of the live brain ECS require brain preparations that best preserve cellular architectures. In that respect, we used acute brain slices as opposed to other preparations that poorly preserve native tissue organization such as cultured neurons or organotypic slices. Moreover, the imaging modality must reach spatial resolutions beyond the diffraction limit as well as tissue access deeper than the first 2–3 pyramidal cell layers inside the slice (>~30 μm) to avoid regions affected during slicing. To this end, deep tissue localization microscopy that is based on tracking the successive positions of single nano-emitters while they explore brain tissues represents a unique approach.

Near-infrared luminescent single-walled carbon nanotubes (SWCNTs) were previously proposed as unique probes for ensemble imaging in the whole animal[11,12] due to their brightness, photostability and spectral imaging range[13,14], as well as for intracellular single molecule tracking in cultured cells[15,16]. It was also shown, at the ensemble level, that their unusual length-to-diameter aspect ratios enhance their penetration within multicellular tumour spheroids depending on the encapsulation agents used[17,18]. In fact, in contrast to spherical nanoparticles, SWCNTs have two characteristic dimensions that impact their diffusion behaviours. Their small diameter (nanometre scale) confers a remarkable accessibility in complex environments, while the combination of their length and rigidity can moderate their diffusion rates to be compatible with video-rate single-molecule imaging[19].

SWCNTs were delivered into young rat brains by the injection of a small volume (5 μl, 3 μg ml$^{-1}$) of solubilized nanotubes into the lateral cerebroventricles (Fig. 1a)[20]. This SWCNT delivery method generates minimal tissue inflammation as the gross morphology and density of the microglial cells—the resident macrophages of the brain—were found to be similar in buffer- and SWCNT-injected brains (Supplementary Fig. 1). SWCNTs coated with phospholipid-polyethylene glycol (PL-PEG) were used because they display low cytotoxicity compared with other encapsulation methods used for luminescent SWCNTs[21,22]. Rats were killed 30 min after the ventricular injection and acute brain slices were prepared for observation under a wide-field fluorescent near-infrared microscope (Fig. 1b). The wavelengths of excitation (845 nm to excite (6,5) SWCNTs at a phonon sideband[23]) and emission (986 nm for (6,5) SWCNTs) are in the transparency window of the studied brain tissues (Fig. 1c) and as such minimize tissue phototoxicity (Supplementary Figs 2 and 3). Phonon sideband excitation also ensures better emission photostability[23] compared with the high photon-energy excitation commonly used to excite SWCNT at their second-order electronic transition (Supplementary Fig. 4).

Single luminescent (6,5) SWCNTs were detected in diverse areas of sagittal brain slices (for example, the neocortex, hippocampus, striatum) (Supplementary Fig. 5). Imaging was performed at different depths in the brain slices, from a few tens of micrometres to avoid the damaged superficial layers up to ~100 μm (Supplementary Fig. 6). The broad SWCNT dissemination away from cerebroventricular injection site was facilitated by their nanometre diameters, and also suggests that SWCNTs were primarily located in the ECS since such a large dissemination would not be possible if SWCNTs were internalized in brain cells. The diffusion of molecules in the ECS is thought to be globally governed by several parameters, such as the geometric path length, trapping in dead-space domains and ECS viscosity due to molecular crowding and transient molecular interactions. At a macroscopic scale, these parameters participate to the so-called tortuosity of the ECS[2,24]. Many SWCNTs were found immobilized away from the ventricular injection zones, probably as a result of non-specific interactions with molecules of the ECS (although the PL-PEG coating minimizes this effect in live cell cultures (Supplementary Fig. 7) and live animals[21]) and/or the existence of dead-space microdomains[2]. The direct observation of PL-PEG-coated SWCNT trapping is thus consistent with the existence of dead-space domains in the ECS. To further ascertain

[1]Laboratoire Photonique Numérique et Nanosciences, Univ. Bordeaux, UMR 5298, F-33400 Talence, France. [2]Institut d'Optique & CNRS, LP2N UMR 5298, F-33400 Talence, France. [3]Univ. Bordeaux, Interdisciplinary Institute for Neuroscience, UMR 5297, F-33000 Bordeaux, France. [4]CNRS, IINS UMR 5297, F-33000 Bordeaux, France. †These authors contributed equally to this work. *e-mail: laurent.cognet@u-bordeaux.fr; laurent.groc@u-bordeaux.fr

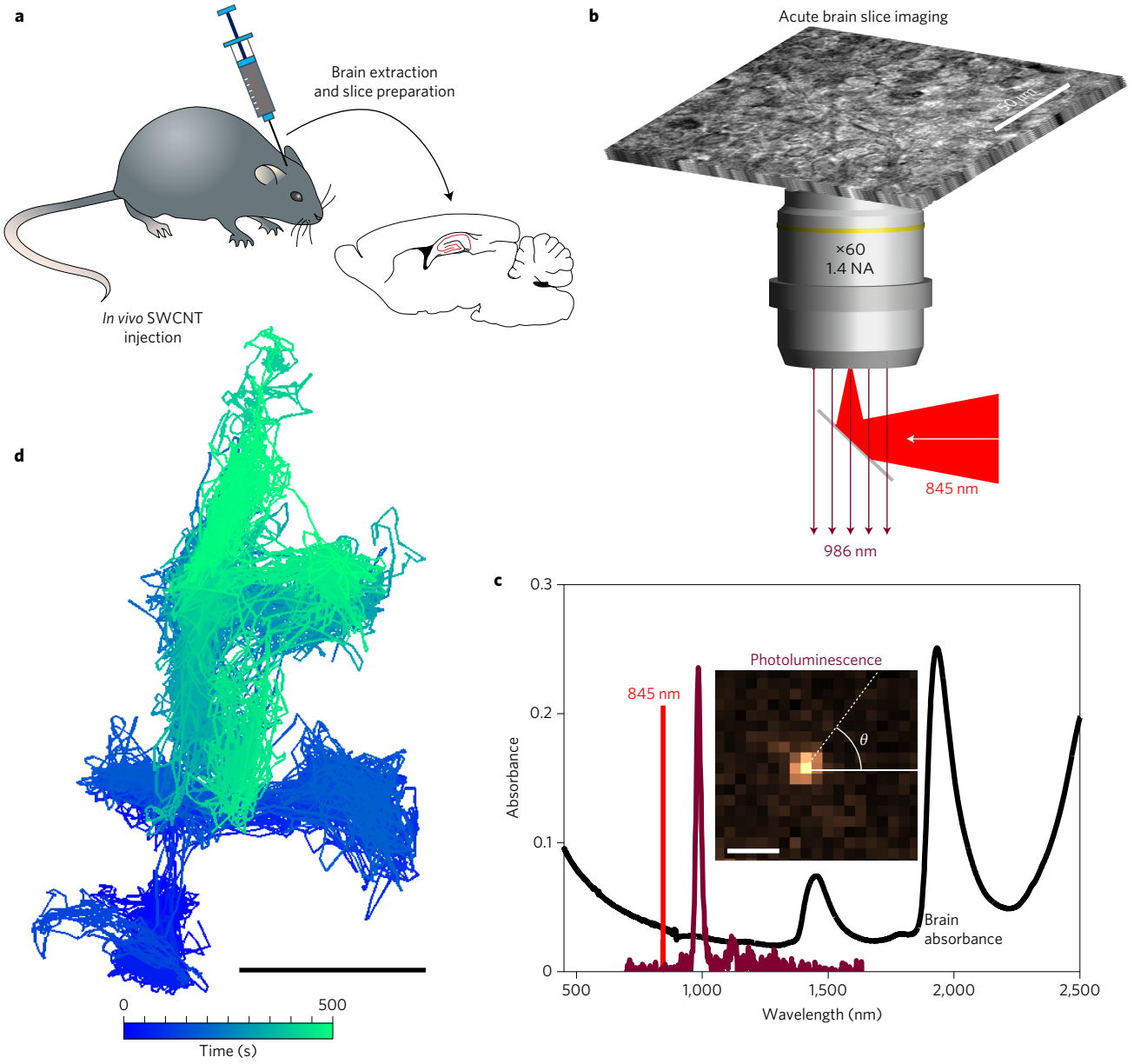


**Figure 1 | Single-molecule tracking of luminescent SWCNTs in live ECS brain tissue. a**, SWCNTs are injected into the lateral ventricles of living rats and diffuse into the neocortex. **b**, Luminescent SWCNTs are imaged in brain slices. **c**, Absorbance spectrum of 1 mm thick brain slice (black) and photoluminescence spectrum of a single (6,5) SWCNT in the ECS (purple) on 845 nm laser excitation (red). Inset, photoluminescence image of a (6,5) SWCNT recorded in the ECS with its orientation $\theta$. **d**, Colour-coded trajectory of a single SWCNT diffusing in live ECS (20,000 data points). Scale bars, 1 µm.

the extracellular location, we directly loaded SWCNTs within hippocampal pyramidal neurons through a patch-clamp pipette. The behaviours of the detected intracellular SWCNTs were distinct from cerebroventricular-injected ones (Supplementary Fig. 8), providing further support for the SWNCTs imaged after intra-cerebroventricular (ICV) injection being primarily extracellular.

The movements of individual SWCNTs exploring the ECS could be resolved with video-rate fluorescence imaging (Fig. 1d). This is primarily due to the high aspect ratio and rigidity of the SWCNTs, linked to their nanometre diameters, which considerably slows down their diffusion in the ECS maze compared with nanometre-sized probes or fully flexible polymers. We checked that small isotropic fluorescent probes diffuse too quickly in the ECS to be imaged at video rate for a long time (observed trajectories <1 s, Supplementary Fig. 9). In addition, we could record long movies of single SWCNT $(x,y)$ diffusion occurring over more than 20,000 frames within the ~1 µm depth-of-focus of the microscope (Supplementary Movie 1). By means of a two-dimensional asymmetric Gaussian fitting analysis, we extracted in each movie frame $i$ the localization of the nanotube centre-of-mass $(x_i, y_i)$ in the imaging plane with subwavelength precision (~40 nm) and the orientation of the nanotube axis $\theta_i$ relative to the $x$ axis in the laboratory frame (Fig. 1c, inset). At any time, SWCNT displacements $r$ can thus be calculated as the distance traveled by the nanotube during a given time lag (see Fig. 2a). Analysis of the fitted 2D Gaussian asymmetry provides a measure of the nanotube lengths $L$, which range here from ~490–780 nm. These lengths match the typical SWCNT lengths of the injected solution as determined by atomic force microscopy (AFM) imaging (Supplementary Fig. 10). Assuming characteristic ECS dimensions $\xi$ larger than 50 nm, these SWCNTs behave as rigid rods in the ECS and their diffusion should be independent of flexibility[19]. The movements of the nanotubes along $(\parallel)$ and perpendicular $(\perp)$ to their axes were then decoupled to calculate two one-dimensional mean squared displacements

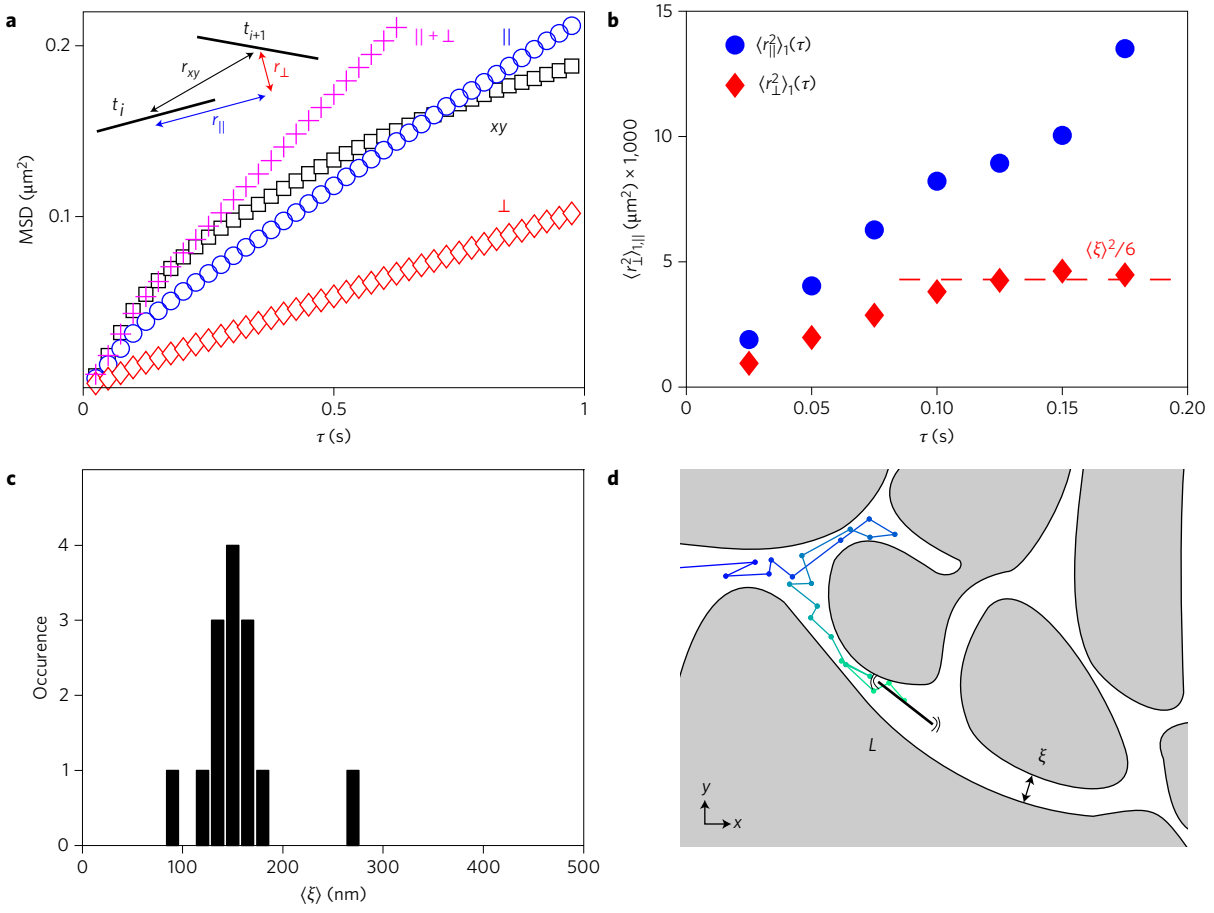


**Figure 2 | SWCNT diffusion properties in the ECS. a**, $MSD_{x,y}(\tau)$ in the laboratory frame and $MSD_{\parallel,\perp}(\tau)$ calculated along and perpendicular to the SWCNT axis for a 2D trajectory recorded in the ECS. Purple crosses correspond to $MSD_{\parallel} + MSD_{\perp}$. **b**, Evolution of the mean MSDs for the slow diffusion states $\langle r^2_{\parallel,\perp}\rangle_1(\tau)$ retrieved from the analysis of the DSDs. The plateau of $\langle r^2_{\perp}\rangle_1(\tau)$ gives an average $\langle\xi\rangle$ of 160 nm. **c**, Histograms of $\langle\xi\rangle$ values measured from all single SWCNT trajectories as in **b**. **d**, Schematic representation of a SWCNT of length *L*, diffusing in the ECS.

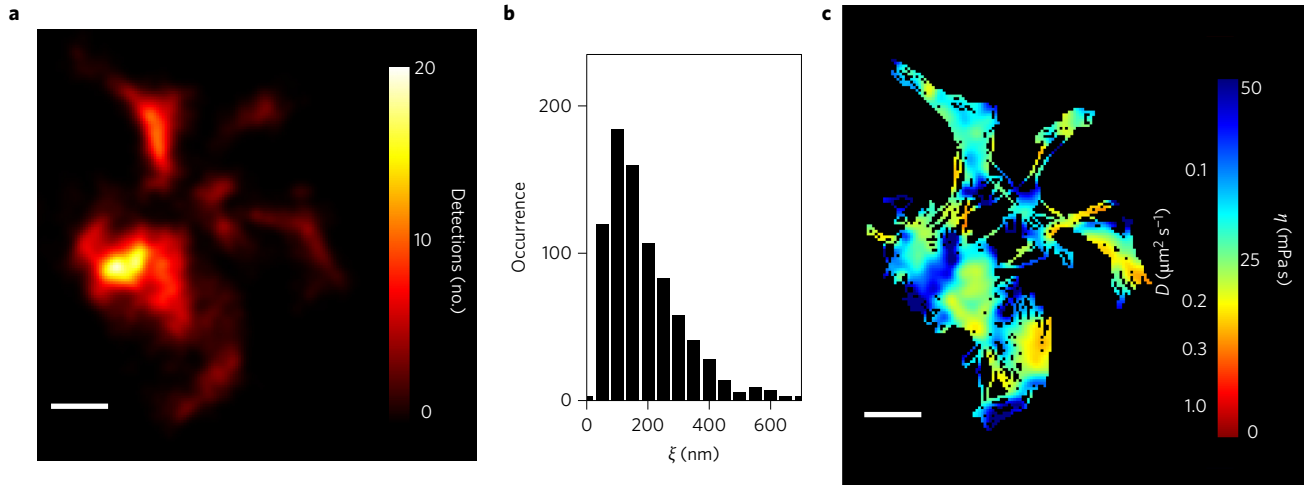


**Figure 3 | Super-resolution imaging of ECS morphology and local ECS viscosity maps. a**, Super-resolved image of live brain ECS morphology obtained from 20,000 localizations of a diffusing SWCNT. Scale bar, 500 nm. **b**, Histogram of $\xi$ ($N = 419$) from 14 super-resolved ECS images as in **a**. **c**, Spatial map of the instantaneous diffusion coefficients of the SWCNTs calculated along the same trajectory using a sliding window of 300 ms. This representation also constitutes a high-resolution spatial map of ECS viscosities (see scale bar).

$MSD_{\parallel}$ and $MSD_{\perp}$ as a function of time (Fig. 2a). The $MSD_{xy}$ corresponding to the 2D movements in the laboratory frame was also calculated. On short timescales ($t \lesssim 200$ ms), $MSD_{xy}$ is linear with time and $MSD_{xy} \approx MSD_{\parallel} + MSD_{\perp}$, whereas for longer timescales $MSD_{xy}$ levels off and $MSD_{\parallel} + MSD_{\perp}$ is close to linear, such that $MSD_{xy} < MSD_{\parallel} + MSD_{\perp}$ (Fig. 2a). The different behaviours of $MSD_{xy}$ and $MSD_{\parallel} + MSD_{\perp}$ indicate that nanotube movements are not free[25] and are thus constrained by the local ECS environment.

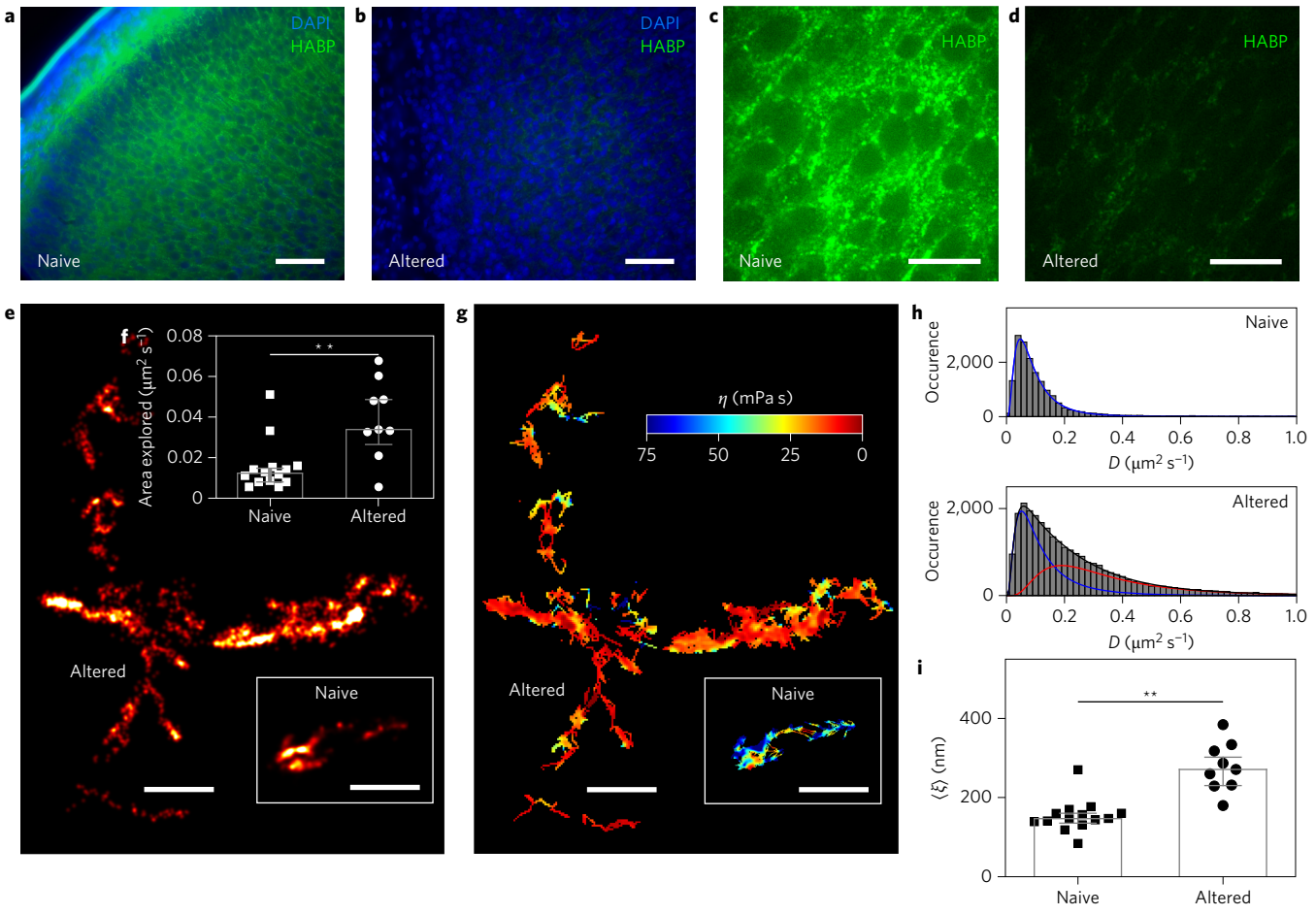


**Figure 4 | Local modifications of the ECS in chemically altered brains. a**,**b**, Representative images of HAPB immunostaining in brain slices from naive (**a**) and hyaluronidase-injected rats (**b**). Neuronal nuclei are labelled with DAPI (blue). Scale bar, 250 μm. **c**,**d**, High-magnification spinning-disk microscope images of HAPB staining in both conditions are also presented. Scale bar: 20 μm. **e**, Examples of super-resolved ECS images of naive versus altered live brain tissues. Scale bar, 2 μm. **f**, Areas explored normalized by SWCNT trajectory lengths. Bars represent the medians of the distributions while the whiskers correspond to the 25th and 75th percentiles of the distributions. **g**, Corresponding spatial viscosity maps. **h**, Histograms of all instantaneous diffusion coefficients. In naive brains the distribution is fitted with a single lognormal distribution (0.08 ± 0.08 μm$^2$ s$^{-1}$, median ± s.d.) while in altered brains, two independent lognormal distributions are needed (0.09 ± 0.11 μm$^2$ s$^{-1}$ and 0.28 ± 0.26 μm$^2$ s$^{-1}$). **i**, $\langle\xi\rangle$ as in Fig. 2e for the two conditions. Bars represent the medians of the distributions while the whiskers correspond to the 25th and 75th percentiles of the distributions. Statistical tests are two-tailed unpaired Mann–Whitney *t*-tests. $^{**}P < 0.01$.

The deviation from linearity of $MSD_{xy}$ also suggests that $t_c \approx 200$ ms represents a characteristic timescale at which SWCNTs explore single ECS subdomains.

Because MSD values calculated from full trajectories inherently reflect average displacements, the properties of transient diffusive states cannot be retrieved by the direct analysis of $MSD_{xy}$, $MSD_{\parallel}$ or $MSD_{\perp}$. To access the transient diffusive states in local environments, we used an analysis based on the distribution of squared displacements (DSD)[26,27] along and perpendicular to the nanotube axis $DSD_{\tau}(r^2_{\parallel,\perp})$ defined for different time lags $\tau$ where $\tau < t_c$ (Supplementary Information). Along each direction ($\parallel$, $\perp$), two diffusion behaviours are found to be characterized by the time dependence of their mean MSD values denoted $\langle r^2_{\parallel,\perp}\rangle_j(\tau)$, where $j = 1$ corresponds to the slowest SWCNT diffusive states and $j = 2$ to faster ones (Supplementary Fig. 11). The population of small displacements perpendicular to the axis of the SWCNTs is bounded, as indicated by the fast saturation of $\langle r^2_{\perp}\rangle_1(\tau)$ (Fig. 2b) while other states mostly display unrestricted diffusion (Fig. 2b and Supplementary Fig. 11). This behaviour can be related to successive diffusion episodes occurring in different ECS confinement domains (see below). The plateau of $\langle r^2_{\perp}\rangle_1(\tau)$, which equals $\langle\xi\rangle^2/6$ for confined diffusion along a 1D coordinate[28], provides a measure of $\langle\xi\rangle$ that represents the average confining ECS dimension (Fig. 2b). As displayed in Fig. 2c, $\langle\xi\rangle$ ranges from 80 to 270 nm (150 ± 40 nm, mean ± s.d.). This dynamic analysis demonstrates that the anisotropic diffusion behaviours of single SWCNTs locally probe the brain ECS and can reveal nanoscale dimensions (Fig. 2d).

Using a similar approach to single-molecule localization microscopy[29], a large number of nanotube localization coordinates obtained with subdiffraction precisions were pooled to create a super-resolved image of the ECS (Fig. 3a). Such images directly unveil the spatial, nanoscale and structural tortuosity of the live brain ECS. The ECS maze is heterogeneous and consists of many connected submicrometre structural domains of various sizes. A total of 419 ECS domains were identified with typical dimensions $\xi$ ranging from ~50 to 700 nm (Fig. 3b and Supplementary Fig. 12). It is worth noting that the ECS nanoscale dimensions and morphologies described here in live brain samples resemble the ECS morphology visualized by electron microscopy following cryofixation of brain tissue[8,9] (Supplementary Fig. 13). Maps of the instantaneous diffusion constants calculated along nanotube trajectories on 300 ms sliding time windows were constructed (Fig. 3c) to evaluate the spatial dependence of the local SWCNT diffusion in live brain tissue. Using the known nanotube lengths, high-resolution

spatial maps of the ECS viscosity were also obtained (Fig. 3c and Supplementary Movie 1). Viscosity values ranged from ~1 to 50 mPa s, which is up to two orders of magnitude larger than that of the cerebrospinal fluid. These viscosity maps reveal that local viscosity of the ECS is spatially inhomogeneous. Interestingly, within this viscosity range the instantaneous diffusion constants of quantum dots in the ECS (which have hydrodynamic diameters of 35 nm) would locally vary from ~0.1 to 10 μm $s^{-1}$. As expected, the average diffusion constant of such quantum dots (~0.1 μm $s^{-1}$) previously observed on macroscopic spatial scales in the ECS[24] is constrained towards the smallest local values and cannot divulge the diversity of local viscosities. By comparing Fig. 3a,c, the spatial dependence of the rheological properties of the ECS indicates that local ECS viscosity values do not correlate with ECS dimensions. Indeed, although $\xi$ values span up to two orders of magnitude, the instantaneous diffusion constants of the SWCNTs vary over up to three decades independently of the ECS dimensions in which the SWCNTs are diffusing. Although bearing diffusion properties that are not necessarily identical to those of endogenous molecules diffusing in the brain ECS, our findings demonstrate that SWCNT tracking unveils and quantifies the diversity of the nanoscale diffusive environments that comprise the ECS. Interestingly, considering the ECS as a fluidic connected space with specialized functional regions[2,4], our results indicate that local structural dimensions are not solely responsible for the variation in the molecular diffusion properties of the ECS. It follows that other mechanisms, including fine-tuned molecular interactions that involve constitutive components of the ECS, must play important roles in controlling the local diffusion of endogenous signalling molecules or nutrients, for example, in local areas of interest.

To corroborate this hypothesis, we then biochemically altered the ECS structure by injecting hyaluronidase into the lateral brain ventricles of young rats several hours before nanotube injection and imaging, a time period that should be sufficient to significantly digest hyaluronic acid[30]. Alterations of the ECM components in the hyaluronidase-injected brains were confirmed by a strong decrease of both hyaluronan binding protein (HABP) (Fig. 4a–d) and aggrecan immunostaining (Supplementary Fig. 14). It is worth noting that we did not observe any modification of the morphology of the neuronal soma or the overall cellular density in hyaluronidase-injected brains at spinning-disk confocal resolution. Analysis of SWCNT diffusion indicates that they explored wider areas compared with naive brains within identical timescales (Fig. 4e,f). Consistent with hyaluronidase-induced disappearance of ECM components, instantaneous diffusion coefficients were significantly increased (calculated as in Fig. 3c), indicating a global reduction in the viscosity of the medium (Fig. 4g,h and Supplementary Movie 2). More precisely, the histogram of diffusion coefficients from naive brains was well fitted by a single lognormal distribution, whereas in the altered brains two lognormal distributions were needed, with one of them being indistinguishable from that used to fit the histogram of naive brains (Fig. 4h). This demonstrates that the effect of hyaluronidase is in fact not spatially homogeneous in the ECS (see also Fig. 4g). The DSD analysis shows that the ECS dimensions explored by SWCNTs were characterized by a moderate but significant increase of mean $\langle\xi\rangle$ in altered brain tissue (280 ± 60 nm) compared with naive tissue (150 ± 40 nm) (Fig. 4i). This indicates that on profound but non-uniform alteration of the ECM, the topology of the ECS offers larger territories for nanoscale molecular exploration by SWCNTs.

Here we provide a new approach that reveals the dimensions and viscosity of the ECS at the nanoscale in the live brain tissue of young rats. The ECS is found to be a maze of interconnected polymorphic compartments that are structured down to the nanoscale and bear specific rheological properties. This knowledge will influence our understanding of chemical-based cellular communication in brain physiology and pathology. In addition, detailed knowledge of the nanoscale ECS network should also foster new strategies for drug delivery.

## Methods

Methods and any associated references are available in the online version of the paper.

Received 18 March 2016; accepted 14 October 2016; published online 21 November 2016

## References


1. Cserr, H. F. *et al.* Extracellular volume decreases while cell volume is maintained by ion uptake in rat-brain during acute hypernatremia. *J. Physiol.* **442,** 277–295 (1991).
2. Syková, E. & Nicholson, C. Diffusion in brain extracellular space. *Physiol. Rev.* **88,** 1277–1340 (2008).
3. Dityatev, A., Schachner, M. & Sonderegger, P. The dual role of the extracellular matrix in synaptic plasticity and homeostasis. *Nat. Rev. Neurosci.* **11,** 735–746 (2010).
4. Xie, L. *et al.* Sleep drives metabolite clearance from the adult brain. *Science* **342,** 373–377 (2013).
5. Lehmenkühler, A., Sykova, E., Svoboda, J., Zilles, K. & Nicholson, C. Extracellular space parameters in the rat neocortex and subcortical white matter during postnatal development determined by diffusion analysis. *Neuroscience* **55,** 339–351 (1993).
6. Metzler-Baddeley, C., Jones, D. K., Belaroussi, B., Aggleton, J. P. & O'Sullivan, M. J. Frontotemporal connections in episodic memory and aging: a diffusion MRI tractography study. *J. Neurosci.* **31,** 13236–13245 (2011).
7. Berezin, V., Walmod, P. S., Filippov, M. & Dityatev, A. Targeting of ECM molecules and their metabolizing enzymes and receptors for the treatment of CNS diseases. *Prog. Brain Res.* **214,** 353–388 (2014).
8. Ohno, N., Terada, N., Saitoh, S. & Ohno, S. Extracellular space in mouse cerebellar cortex revealed by *in vivo* cryotechnique. *J. Comp. Neurol.* **505,** 292–301 (2007).
9. Korogod, N., Petersen, C. C. & Knott, G. W. Ultrastructural analysis of adult mouse neocortex comparing aldehyde perfusion with cryo fixation. *eLife* **4,** e05793 (2015).
10. Verkman, A. S. Diffusion in the extracellular space in brain and tumors. *Phys. Biol.* **10,** 045003 (2013).
11. Welsher, K. *et al.* A route to brightly fluorescent carbon nanotubes for near-infrared imaging in mice. *Nat. Nanotech.* **4,** 773–780 (2009).
12. Heller, D. A. *et al.* Multimodal optical sensing and analyte specificity using single-walled carbon nanotubes. *Nat. Nanotech.* **4,** 114–120 (2009).
13. Bachilo, S. M. *et al.* Structure-assigned optical spectra of single-walled carbon nanotubes. *Science* **298,** 2361–2366 (2002).
14. Cognet, L. *et al.* Stepwise quenching of exciton fluorescence in carbon nanotubes by single-molecule reactions. *Science* **316,** 1465–1468 (2007).
15. Reuel, N. F., Dupont, A., Thouvenin, O., Lamb, D. C. & Strano, M. S. Three-dimensional tracking of carbon nanotubes within living cells. *ACS Nano* **6,** 5420–5428 (2012).
16. Fakhri, N. *et al.* High-resolution mapping of intracellular fluctuations using carbon nanotubes. *Science* **344,** 1031–1035 (2014).
17. Wang, Y., Bahng, J. H., Che, Q., Han, J. & Kotov, N. A. Anomalously fast diffusion of targeted carbon nanotubes in cellular spheroids. *ACS Nano* **9,** 8231–8238 (2015).
18. Jena, P. V. *et al.* Photoluminescent carbon nanotubes interrogate the permeability of multicellular tumor spheroids. *Carbon* **97,** 99–109 (2016).
19. Fakhri, N., MacKintosh, F. C., Lounis, B., Cognet, L. & Pasquali, M. Brownian motion of stiff filaments in a crowded environment. *Science* **330,** 1804–1807 (2010).
20. Varela, J. A. *et al.* Targeting neurotransmitter receptors with nanoparticles *in vivo* allows single-molecule tracking in acute brain slices. *Nat. Commun.* **7,** 10947 (2016).
21. Liu, Z. *et al.* *In vivo* biodistribution and highly efficient tumour targeting of carbon nanotubes in mice. *Nat. Nanotech.* **2,** 47–52 (2007).
22. Gao, Z., Varela, J. A., Groc, L., Lounis, B. & Cognet, L. Toward the suppression of cellular toxicity from single-walled carbon nanotubes. *Biomater. Sci.* **4,** 230–244 (2016).
23. Santos, S. M. *et al.* All-optical trion generation in single-walled carbon nanotubes. *Phys. Rev. Lett.* **107,** 187401 (2011).
24. Thorne, R. G. & Nicholson, C. *In vivo* diffusion analysis with quantum dots and dextrans predicts the width of brain extracellular space. *Proc. Natl Acad. Sci. USA* **103,** 5567–5572 (2006).
25. Han, Y. *et al.* Brownian motion of an ellipsoid. *Science* **314,** 626–630 (2006).
26. Schutz, G. J., Schindler, H. & Schmidt, T. Single-molecule microscopy on model membranes reveals anomalous diffusion. *Biophys. J.* **73,** 1073–1080 (1997).

27. Tardin, C., Cognet, L., Bats, C., Lounis, B. & Choquet, D. Direct imaging of lateral movements of AMPA receptors inside synapses. *EMBO J.* **22,** 4656–4665 (2003).
28. Kusumi, A., Sako, Y. & Yamamoto, M. Confined lateral diffusion of membrane receptors as studied by single particle tracking (nanovid microscopy): effects of calcium-induced differentiation in cultured epithelial cells. *Biophys. J.* **65,** 2021–2040 (1993).
29. Godin, A. G., Lounis, B. & Cognet, L. Super-resolution microscopy approaches for live cell imaging. *Biophys. J.* **107,** 1777–1784 (2014).
30. Kochlamazashvili, G. *et al.* The extracellular matrix molecule hyaluronic acid regulates hippocampal synaptic plasticity by modulating postsynaptic L-type Ca (2+) channels. *Neuron* **67,** 116–128 (2010).

## Acknowledgements

We thank E. Bézard, M. Blanchard-Desce, B. Bontempi and P. Bon for helpful discussions. We thank the Bordeaux Imaging Center (service unit of the CNRS-INSERM and Univ. Bordeaux). We thank J.P. Salvetat for experimental help with AFM imaging and J. Ferreira for support with histological experiments. This work was supported by CNRS, the Agence Nationale de la Recherche (ANR-14-OHRI-0001-01), IdEx Bordeaux (ANR-10-IDEX-03-02), Labex Brain (ANR-10-LABX-43), Conseil Régional d'Aquitaine (2011-1603009) and the France-BioImaging national infrastructure (ANR-10-INBS-04-01). A.G.G. acknowledges financial support from the Fondation pour la Recherche Médicale and the Fonds Recherche du Québec–Nature et Technologies. J.A.V. acknowledges funding from Marie Curie Individual Fellowship 326442.

## Author contributions

A.G.G., J.A.V., Z.G. and J.P.D. performed the experiments. A.G.G., N.D., B.L. and L.C. performed the analysis. B.L., L.G. and L.C. co-supervised the study. L.G. and L.C. designed the study. All authors discussed the results and co-wrote the manuscript.

## Additional information

Supplementary information is available in the online version of the paper. Reprints and permissions information is available online at www.nature.com/reprints. Correspondence and requests for materials should be addressed to L.G. and L.C.

## Competing financial interests

The authors declare no competing financial interests.

## Methods

**SWCNT preparation.** PL-PEG preparation. HiPco synthesized nanotubes (batch no. 195.7 bought from Rice University) were suspended by biocompatible PL-PEG) molecules (#MPEG-DSPE-5000, Laysan Bio, Inc.) that prevent non-specific biomolecule absorption, minimize nanotube sticking and allow nanotube diffusion in live tissue[21,22]: 2 mg of raw SWCNTs and 100 mg PL-PEG were added in 2 ml Milli-Q water and dispersed by tip sonication (6 W output for 3 min). Nanotube bundles and impurities were precipitated by centrifuging the dispersion at 10,000 r.p.m. for 60 min at 4 °C. The supernatant was collected and stored at 4 °C for brain injection within 48 h. The concentration of the PL-PEG SWCNT solution was estimated to be 3 μg ml$^{-1}$. From the two-dimensional photoluminescence excitation/emission map of the injected SWCNT solution (Supplementary Fig. 15), the subpopulation of (6,5) SWCNTs is estimated to represent 3–5% of the total population, such that the SWCNTs detected in the brain slices at low density are not affected by other chiralities.

PL-PEG-$NH_2$ preparation. SWCNTs were also suspended by biocompatible PL-PEG-amine (PL-PEG-$NH_2$) molecules (#MPEG-DSPE-$NH_2$-5000, Laysan Bio, Inc.): 1 mg of raw SWCNTs and 15 mg PL-PEG-$NH_2$ were added in 1 ml Milli-Q water and 0.5 ml deuterium oxide and dispersed by tip sonication (8 W output for 30 s). Nanotube bundles and impurities were precipitated by centrifuging the dispersion at 10,000 r.p.m. for 45 min at 4 °C. The supernatant was collected and stored at 4 °C for experiments (0.4 μg ml$^{-1}$).

**Intraventricular injections.** Sprague–Dawley rats (Janvier) were used for this work, both male and female, treated according to the guidelines of the University of Bordeaux/CNRS Animal Care and Use Committee. The injections of SWCNTs were performed in living Sprague–Dawley rat pups (1–4 days old) anesthetized by hypothermia. Approximately 5 μl of the SWCNT dispersion was injected in each lateral ventricle (12 rats). Under cold light illumination, the injection point was found by first drawing a virtual line between the eye and lambda (easily seen through the skin), finding the midpoint of that line and then moving 2 mm caudal from that midpoint along the virtual line. The injection was performed at that point, at a depth of 2.6 mm for P1 pups, 2.9 mm for P2 pups, 3.1 mm for P3 pups and 3.5 mm for P4 pups. For the hyaluronidase studies the intraventricular injection was performed in the same way (3 rats), injecting hyaluronidase from bovine testes 20 mg ml$^{-1}$ in PBS (Sigma Aldrich #H3506) the night before injecting the SWCNTs.

**Acute brain slices preparation.** Between 10 min and up to 3 h after SWCNT injection, pups were decapitated and parasagittal brain slices (0.5 mm thick) were prepared in an ice-cold artificial cerebrospinal fluid (ACSF) solution containing 126 mM NaCl, 3.5 mM KCl, 2 mM $CaCl_2$, 1.3 mM $MgCl_2$, 1.2 mM $NaH_2PO_4$, 25 mM $NaHCO_3$ and 12.1 mM glucose (gassed with 95% $O_2$:5% $CO_2$; pH 7.35). Slices were then imaged in oxygenated ACSF at 33 °C perfused into the imaging chamber with a peristaltic pump.

**Immunostaining.** Staining of Iba1, Aggrecan and HABP was performed in coronal brain slices of 80 μm thickness. Before antibody incubation, the slices were incubated with PBS-Triton-X100 1 and 4% BSA for 2 h under agitation at room temperature. Slices were subsequently washed three times with PBS for 5 min for each washing. Slices were incubated overnight at 4 °C with primary antibodies in a PBS-Triton-X100 0.2 and 2% BSA solution. Anti-Iba1 rabbit antibody (Wako Pure Chemical Industries #019-19741) was used at a 1:200 dilution. Anti-Aggrecan rabbit antibody (Millipore #AB1031) was used at a 1:200 dilution. Biotinilated HABP (Amsbio #AMS.HKD-BC41) was also used at a 1:200 dilution. Slices were subsequently washed three times with PBS for 5 min each time, and incubated with secondary reagents. Anti-Iba1 and anti-Aggrecan antibodies were labelled with goat anti-rabbit Alexa568 (ThermoFisher Scientific #A-11011) in a PBS-Triton-X100 0.2 and 2% BSA solution for 2 h at room temperature under agitation at a 1:1,000 dilution. Biotinilated HABP was labelled with Alexa568 streptavidin (ThermoFisher Scientific #S11226) in PBS-Triton-X100 0.2 and 2% BSA solution for 2 h at room temperature under agitation, at a 1:1,000 dilution. Slices were finally washed three times with PBS and mounted on glass slides with Vectashield + DAPI (Vector Labs).

**Organotypic slice preparation.** Organotypic slice cultures were prepared as previously described[31]. Briefly, 350 μm thick hippocampal slices were obtained from postnatal day 5 to postnatal day 7 Sprague–Dawley rats using a McIlwain tissue chopper, and were placed in a pre-heated (37 °C) dissection medium containing 175 mM sucrose, 25 mM D-glucose, 50 mM NaCl, 0.5 mM $CaCl_2$, 2.5 mM KCl, 0.66 mM $KH_2PO_4$, 2 mM $MgCl_2$, 0.28 mM $MgSO_4$-$7H_2O$, 0.85 mM $Na_2HPO_4$-$12H_2O$, 2.7 mM $NaHCO_3$ and 0.4 mM HEPES, $2 \times 10^{-5}$ % phenol red, pH 7.3 (all products from Sigma unless specified). After 25 min of incubation, slices were transferred onto white FHLC membranes (0.45 μm) set on Millicell Cell Culture Inserts (Millipore, 0.4 mm; diameter 30 mm), and cultured for up to 14 days on multiwell-plates at 35 °C/5% $CO_2$ in a culture medium composed of 50% Basal Medium Eagle, 25% Hank's balanced salt solution 1X (with $MgCl_2$/with $CaCl_2$), 25% heat-inactivated horse serum, 0.45% D-glucose and 1 mM L-glutamine (all products from Gibco unless specified). The medium was changed every 2–3 days.

**Single-cell electroporation.** The electroporation of single pyramidal neurons was performed as previously described[32]. Briefly, individual CA1 pyramidal neurons from 4–6 day *in vitro* hippocampal slices were electroporated to transfect cDNA encoding EGFP. Plasmids (5 μl at 1 μg μl$^{-1}$) were dissolved in a filtered caesium-based solution containing 135 mM caesium-methanesulfonate, 8 mM NaCl, 10 mM HEPES, 0.2 mM EGTA, 4 mM $Na_2ATP$, 0.33 mM $Na_3GTP$ and 5 mM tetraethylammonium chloride, pH 7.3 (all products from Sigma unless specified). This solution was supplemented with 10 μl of filtered endotoxin-free buffer TE (Qiagen), then centrifuged twice to pull down potential debris (10,000 r.p.m., 15 min, 4 °C) and used to fill 5–6 MΩ borosilicate patch pipettes. Electroporation was performed in 2 ml of pre-warmed (37 °C/5% $CO_2$) HEPES-based ACSF containing 130 mM NaCl, 2.5 mM KCl, 2.2 $CaCl_2$, 1.5 mM $MgCl_2$, 10 mM HEPES and 10 mM D-glucose. Plasmid transfer was allowed by the delivery of 50 μs wide square pulses at 100 Hz (1 s duration; −14 V current amplitude).

**COS-7 cell culture.** COS-7 cells were grown in DMEM without phenol-red (PAN Biotech, P04-01515) supplemented with 10% v/v foetal calf serum (FCS-Dominique Dutscher, 500105) and 1% v/v penicillin/streptomycin (Dominique Dutscher, P06-07100) in 25 ml flasks (Falcon, 353082) at 37 °C, 5% $CO_2$. They were kept below 90% confluence, at which point cells were washed in sterile filtered PBS (PAN Biotech, P04-36500), detached in a small volume of trypsin (PAN Biotech, P10-021100), washed in full warm medium and split 1/10 into a new flask. For imaging, 90% confluent cells were similarly detached with trypsin and diluted 1/10 in full warm medium. COS-7 cells were plated in uncoated petri dishes. 24 h after the plating, nanotubes were added (10 μl of the 3 mg l$^{-1}$ PL-PEG nanotube solution and 60 μl of the 0.4 mg l$^{-1}$ PL-PEG-$NH_2$ nanotube solution) to 1 ml of medium for 1 h. The samples were rinsed three times for 5 min with medium and imaged under the fluorescent microscope.

**Wide-field fluorescence microscopy set-up.** Single-SWCNT photoluminescence imaging was performed with an inverted microscope equipped with an electron-multiplying CCD camera (Princeton Instruments ProEm) and a 1.45 NA ×60 objective in a wide-field geometry. The excitation source consisted of a tunable Ti:Sa laser emitting at a wavelength of 845 nm to preferentially excite (6,5) SWCNTs at the resonance of the dark *K*-momentum exciton[23]. The excitation intensity was kept at 10 kW cm$^{-2}$ with circularly polarized light. A dichroic mirror (FF875-Di01, Semrock) and a long-pass emission filter (ET900LP, Chroma) were used to illuminate and detect the SWCNT-emitted fluorescence. Images of SWCNTs were recorded at 40 or 50 frames per second (typically 20,000 frames). GFP/Alexa488 (excitation: FF02-472/30, dichroic: FF495-Di03 and emission: FF01-520/35) and DAPI (excitation: FF01-387/11, dichroic : FF409-Di03 and emission: FF02-447/60) were imaged using epifluorescence white-light excitation with appropriate filter sets.

**Spinning disk microscope.** Alexa568 imaging in acute slices was performed in a Leica DMI6000 inverted microscope (Leica Microsystems) with a Yokogawa spinning disk unit CSU-X1. The set-up was equipped with a live cell chamber and the temperature was constantly kept at 37 °C. Tissue scans were obtained with either ×10 air, ×63 oil and ×100 oil objectives, with exposure times of 50–100 ms per frame. DAPI staining in fixed tissue was excited with a 405 nm laser line, and detected through a standard DAPI emission filter. Images were acquired using an Evolve EM-CCD camera (Photometrics), setting the EM gain at 600.

**NIR spectrometer set-up.** The emission spectra of single SWCNTs were collected using a cryogenically cooled 1D InGaAs detector (OMA V, Roper Scientific) placed at the output of a 150 mm spectrometer. A Chameleon (coherent) pumped with a Ti:Sapphire laser (spectral range of 530–700 nm) and a Ti:Sa laser (spectral range of 700–850 nm) were used to generate a two-dimensional photoluminescence excitation/emission map of the PL-PEG SWCNT solution. Individual spectra of the nanotube solution, in a 1 cm long quartz cuvette, were normalized by the incident power. The spectrum of a solution containing only surfactant, acquired under the same experimental condition, was subtracted for each laser wavelength. The proportion of (6,5) nanotubes in the solution was estimated by comparing the peak value for the detected semiconducting chiralities and assuming ~30% of metallic chiralities in HiPco samples.

**Single-cell loading.** Single CA1 pyramidal neurons from 4–8 days *in vitro* (div) hippocampal organotypic slices were loaded with dilutions of carbon nanotubes to allow monitoring of patterns of intracellular motion. Briefly, nanotubes were dissolved (1/100 dilution) in a filtered caesium-based solution containing 135 mM caesium-methanesulfonate, 8 mM NaCl, 10 mM HEPES, 0.2 mM EGTA, 4 mM $Na_2ATP$, 0.33 mM $Na_3GTP$, 5 mM tetraethylammonium chloride, pH 7.3 (all products from Sigma unless specified). This solution was supplemented with Alexa-488 (20 μg ml$^{-1}$) to allow further visual detection of the neurons of interest and used to fill 5–6 MΩ borosilicate patch pipettes. Single-cell loading was performed in 2 ml of pre-warmed (37 °C/5% $CO_2$) HEPES-based artificial cerebrospinal fluid (ACSF) containing 130 mM NaCl, 2.5 mM KCl, 2.2 mM $CaCl_2$, 1.5 mM $MgCl_2$, 10 mM HEPES, 10 mM D-glucose. Nanotube transfer from the caesium-based solution to the cytoplasm was allowed by patching pyramidal neurons in whole-cell configuration.

**Determination of SWCNT localization and orientation.** Two-dimensional Gaussian functions with an arbitrary orientation were used to fit SWCNT images using custom MatLab routines and determine SWCNT localizations ($x_i$, $y_i$), orientation $\theta_i$, as well as the large and small radii of the SWCNT image. Four consecutive images were averaged for each fit to improve the localization precision (40 nm). SWCNT coordinates are then interconnected to reconstruct nanotube trajectories. When available, the position of an immobile SWCNT was used to correct eventual small stage drifts over the 10 min recordings. Orientations ($\theta \in [0, \pi]$) obtained from the Gaussian fits are by construction doubly degenerate. The SWCNT orientation on the first image of the movie is assumed to be between $[0, \pi]$. This choice dictates which end of the SWCNT is considered the front of the tube. For all other orientations, continuity arguments are used to remove this degeneracy and to allow the orientation to be a real unbounded physical quantity ($\theta \in [-\infty, \infty]$).

**Super-resolved images of the ECS from SWCNT localizations.** For each trajectory, a super-resolved image of the ECS was computed by cumulating all of the SWCNT localizations (typically 20,000 points). In super-resolved images, each localization is displayed a two-dimensional Gaussian of 50 nm width and unit amplitude as commonly used in localization microscopy[29].

**Estimation of SWCNT lengths.** For each SWCNT trajectory imaged in live brain ECS, the distribution of the eccentricity, obtained from the 2D asymmetric Gaussian fits of the nanotube images, was calculated when nanotube movements were undetectable (displacements between images <40 nm). For each trajectory, the mean of the distribution was then used to determine the nanotube length (Supplementary Fig. 10) by comparison with the following model: the photoluminescence profile of a rigid nanotube of varying length $L$ emitting at 986 nm was modelled as done previously[33] using an exciton diffusion length of ~100 nm to provide a look-up table.

**AFM.** PL-PEG SWCNTs were spin-coated on plasma-cleaned glass coverslips using a G3P-8 spin coater (Specialty Coating Systems) at 930 r.p.m. for 3 min. To remove excess PL-PEG, samples were rinsed using Milli-Q water. AFM images were recorded using an 8 nm diameter $Si_3N_4$ tip (Supplementary Fig. 10b,c). For each well-isolated SWCNT, the length was quantified using the NeuronJ plugin in ImageJ[34].

**MSD analysis.** For each trajectory, three MSD curves were calculated as exemplified in Fig. 2a: (i) $MSD_{xy}$ in the laboratory frame corresponding to 2D movements in the imaging plane, and (ii) $MSD_{\parallel}$ and $MSD_{\perp}$ by decoupling 1D movements ($\parallel$) and ($\perp$) to the nanotube axis.

To decouple the diffusion of SWCNTs along and perpendicular to their principal axis, the displacement vector $(x_{i+1} - x_i, y_{i+1} - y_i)$ was determined at time $t_{i+1}$ from the projection on the nanotube orientation vector obtained at time $t_i$ (see inset of Fig. 2a). This procedure to decouple the movements along and perpendicular to anisotropic object axis was presented previously[19,25]. One-dimensional $MSD_{\parallel}$ and $MSD_{\perp}$ could then be calculated from decoupled displacements (Fig. 2a).

For one-dimensional free diffusion, MSD curves are linear with time, with a slope equal to $2D$. More precisely, $MSD(\tau) = \langle r^2 \rangle(\tau) = \int_{-\infty}^{+\infty} x^2 c(x, \tau) dx = 2D\tau$, where $D$ is the diffusion coefficient and $c(x, t)$ represents the probability of finding nanotubes at position $x$ at time $t$ if all of the nanotubes were initially placed at $x = 0$. $c(x, t)$ is the solution to the one-dimensional diffusion equation $(\partial c(x, t))/(\partial t) = D((\partial^2 c(x, t))/(\partial x^2))$ and equals $c(x,t) = (N/\sqrt{4\pi Dt})e^{-x^2/4Dt}$, where $N$ is the number of particles in the system.

Similarly, for two-dimensional free diffusion, the MSD slope is equal to $4D$ since the MSD equals $MSD(\tau) = \langle r^2 \rangle(\tau) = \int_0^{+\infty} \rho^2 c(\rho, \tau) d\rho = 4D\tau$ where $c(\rho, t)$ is the solution of the two-dimensional diffusion equation.

When the MSDs are not linear with time, a diffusion coefficient can be defined from the initial slopes of $\langle r^2 \rangle(\tau)$ determined on short timescales.

**DSD and calculation of $\langle \xi \rangle$.** Considering a diffusing particle, the cumulative distribution of squared displacements ($DSD^{\tau}(r^2)$) represents the probability of finding the particle at a distance less than $r$ from its initial position after a time lag $\tau$ (Figs 2b,c, 4i and Supplementary Fig. 11).

In the case of a freely diffusing particle along one coordinate, it is given by:

$$DSD^{\tau}(r^2) = \frac{\int_{-r}^{+r} c(x, \tau) dx}{\int_{-\infty}^{+\infty} c(x, \tau) dx} = \mathrm{erf}(\sqrt{r^2/4D\tau}) = \mathrm{erf}(\sqrt{r^2/2\langle r^2 \rangle(\tau)})$$

In the case of a mixture of particles following two distinct 1D diffusion behaviours (for example, free diffusion with $D_1$ and $D_2$), the DSD is characterized by summing two independent diffusive processes:

$$DSD^{\tau}(r^2) = \sum_{i=1}^{2} \alpha_i \, \mathrm{erf}\left(\sqrt{r^2/2\langle r^2 \rangle_i(\tau)}\right) \quad (1)$$

where $\alpha_i$ are the fraction of particles in the different diffusive states (in the case of free diffusion $\langle r^2 \rangle_i(\tau) = 2D_i\tau$).

A similar analysis was previously used to retrieve different molecular populations bearing distinct 2D diffusion behaviours from the observation of many short trajectories[26,27].

Here a single and long trajectory of a diffusing SWCNT that displays different temporal diffusive behaviours along its course is analysed. To retrieve the different diffusive behaviours, the DSD analysis was performed on the displacements along and perpendicular to SWCNT axis.

From single trajectories, the cumulative DSD along each direction (parallel and perpendicular to the nanotube axis) was computed for every time lag (see examples in Supplementary Fig. 11 for the trajectory analysed in Figs 2 and 3). Each line corresponds to the experimental DSDs at a given $\tau$. Values of $\alpha_j$ and $\langle r^2 \rangle_j$ were estimated by fitting equation (1) in each line. Two different diffusing processes were systematically retrieved from the global fitting procedure along each direction ($\langle r^2_{\perp,\parallel} \rangle_{1,2}$). The evolutions $\langle r^2_{\perp,\parallel} \rangle_{1,2}$ are presented in Supplementary Fig. 11c,d as a function of $\tau$.

The evolution of $\langle r^2_1 \rangle_{\perp}$ is the slowest and displays a saturation revealing a confinement of the transverse movements of SWCNTs in the ECS. The typical ECS dimension responsible for this confinement can be estimated from the saturation value of $\langle r^2_{\perp} \rangle_1$: $\xi = \sqrt{6\langle r^2_{\perp} \rangle_1^{\mathrm{sat}}}$[28].

**2D spatial maps of instantaneous diffusion coefficients and local ECS viscosity.** To create diffusion coefficient spatial maps, MSDs were calculated in the laboratory frame using a sliding window of 300 ms along each trajectory instead of the full trajectory as above (Figs 3c, 4g,h and Supplementary Movies 1 and 2). Linear fits of the initial slopes of the sliding MSDs were performed on the first 100 ms to obtain the instantaneous diffusion coefficients $D_{xy}$ as a function of time. The values of the instantaneous diffusion coefficients were obtained for each subset of detections ($t_0 - 150$ ms $\leq t \leq t_0 + 150$ ms) and associated with the centroid position (Figs 3c and 4e,g,h). Maps were created using pixels of 25 nm. Instantaneous diffusion coefficients falling within the same pixel were averaged. For visualization purposes, convolution with a 2D Gaussian of 50 nm FWHM was applied to smooth the data.

To link instantaneous diffusion coefficient values of the SWCNTs to local viscosities of the ECS, we used the relationship between the diffusion coefficient of highly anisotropic rods diffusing in a 2D plane and the viscosity[35]: $\eta = (3k_BT\ln(\phi))/(8\pi D_{xy}L)$, where $k_B$ is the Boltzmann constant and $T$ is temperature. The nanotube length was estimated for each trajectory using the eccentricity of the imaged nanotube (see above).

**Estimation of the ECS dimensions from the analysis of super-resolved images.** Super-resolved images revealed the diversity and complexity of the morphology of the ECS. To measure the typical dimensions of the ECS, we applied a global analysis by using a set of 2D Gaussian functions to directly fit the SWCNT localizations used to create the super-resolved images (Supplementary Fig. 12b). Initial guesses for applying Gaussian fitting were based on local density maxima of the nanotube localizations (Supplementary Fig. 12a, inset and c). Two maxima that less than 75 nm apart could not induce two different Gaussian functions. The transverse dimensions of the set of 2D Gaussian functions used to fit the nanotube localizations provides the dimensions $\xi$ of the ECS displayed in Fig. 3b and Supplementary Fig. 12a.

**Code availability.** Analysis codes used in this study are available upon request to L.C. or L.G.

## References


31. Stoppini, L., Buchs, P. A. & Muller, D. A simple method for organotypic cultures of nervous tissue. *J Neurosci. Methods* **37,** 173–182 (1991).
32. Haas, K., Sin, W. C., Javaherian, A., Li, Z. & Cline, H. T. Single-cell electroporation for gene transfer in vivo. *Neuron* **29,** 583–591 (2001).
33. Oudjedi, L., Parra-Vasquez, A. N., Godin, A. G., Cognet, L. & Lounis, B. Metrological investigation of the (6,5) carbon nanotube absorption cross section. *J. Phys. Chem. Lett.* **4,** 1460–1464 (2013).
34. Meijering, E. *et al.* Design and validation of a tool for neurite tracing and analysis in fluorescence microscopy images. *Cytometry A* **58,** 167–176 (2004).
35. Han, Y., Alsayed, A., Nobili, M. & Yodh, A. G. Quasi-two-dimensional diffusion of single ellipsoids: aspect ratio and confinement effects. *Phys. Rev. E* **80,** 011403 (2009).